

# Implications of a Hot Atmosphere/Corino from ALMA Observations toward NGC 1333 IRAS 4A1

Dipen Sahu<sup>1,2,3</sup>, Sheng-Yuan Liu<sup>2</sup>, Yu-Nung Su<sup>2</sup>, Zhi-Yun Li<sup>4</sup>, Chin-Fei Lee<sup>2</sup>, Naomi Hirano<sup>2</sup>, and Shigehisa Takakuwa<sup>2,5</sup> hIndian Institute of Astrophysics, Sarjapur Main Road, 2nd Block, Koramangala, Bangalore-560034, India; dipen.sahu@iiap.res.in

Academia Sinica Institute of Astronomy and Astrophysics, 11F of AS/NTU Astronomy-Mathematics Building, No.1, Section 4, Roosevelt Rd, Taipei 10617, Taiwan, R.O.C.

<sup>3</sup> Physical Research Laboratory, Ahmedabad-380009, India

<sup>4</sup> Astronomy Department, University of Virginia, Charlottesville, VA 22904, USA

#### Abstract

We report high angular resolution observations of NGC 1333 IRAS 4A, a protostellar binary including A1 and A2, at 0.84 mm with the Atacama Large Millimeter/submillimeter Array. From the continuum observations, we suggest that the dust emission from the A1 core is optically thick, and A2 is predominantly optically thin. The A2 core, exhibiting a forest of spectral lines including complex molecules, is a well-known hot corino, as suggested by previous works. More importantly, we report, for the first time, solid evidence of complex organic molecules (COMs), including CH<sub>3</sub>OH, <sup>13</sup>CH<sub>3</sub>OH, CH<sub>2</sub>DOH, and CH<sub>3</sub>CHO, associated with the A1 core seen in absorption. The absorption features mostly arise from a compact region around the continuum peak position of the A1 core. Rather than originating from a larger common envelope surrounding the protobinary, the COM features are associated with individual cores A1 and A2. Considering the signatures observed in both continuum and spectral lines, we propose two possible scenarios for IRAS 4A1: the COM absorption lines may arise from a hot-corino-like atmosphere at the surface of an optically thick circumstellar disk around A1, or the absorption may arise from different layers of a temperature-stratified, dense envelope.

Key words: astrochemistry – ISM: abundances – ISM: individual objects (NGC 1333 IRAS 4A) – ISM: molecules – stars: formation

## 1. Introduction

Hot cores and hot corinos are associated with (high- and low-mass) star formation at its relatively early stage of evolution. Due to the high temperature in the vicinity of a protostar, a large abundance of complex organic molecules (COMs, containing typically at least six atoms; Herbst & van Dishoeck 2009) are observed in the gas phase. Hot cores, with typical sizes of <0.1 pc, densities of  $>2 \times 10^7$  cm<sup>-3</sup>, and temperatures of >100 K (e.g., van der Tak 2004), are related to massive star-forming regions. Orion KL, for example, hosts an archetypal hot molecular core, as revealed by millimeter molecular line observations (e.g., Blake et al. 1987). Similar spectral line surveys found that saturated COMs, such as CH<sub>3</sub>OH, HCOOCH<sub>3</sub>, and CH<sub>3</sub>OCH<sub>3</sub>, are especially abundant in the hot core regions (e.g., Comito et al. 2005; Tercero et al. 2010; Crockett et al. 2014). The low-mass analogs of the hot cores are dubbed as hot corinos. NGC 1333 IRAS 4A (IRAS 4A hereafter) and IRAS 16293-2422 (I16293 hereafter) are among the first recognized hot corinos (Cazaux et al. 2003; Bottinelli et al. 2004). There are only a handful of hot corinos known to date (e.g., Bottinelli et al. 2007; Öberg et al. 2011, 2014; Fuente et al. 2014).

The observed COMs in hot cores and hot corinos have often been suggested to form primarily in icy mantles of grains and later are liberated into the gas phase by thermal evaporation (desorption; Millar et al. 1991; Charnley et al. 1992). Further investigation indicated, though, that their formation, through a recombination of radicals on grain surfaces during the warm-up phase in the star formation process, may be as important (Garrod & Herbst 2006). Laboratory experiments and theoretical calculations, nevertheless, demonstrated that methanol is

produced largely in the grain phase through repeated hydrogenation of CO (e.g., Tielens & Hagen 1982; Tielens 2005), as follows:

$$CO_{surface} \xrightarrow{H} HCO_{surface} \xrightarrow{H} CH_{3}O_{surface} \xrightarrow{H} CH_{3}OH_{surface}. \quad (1)$$

Gas-phase production of  $CH_3OH$ , on the other hand, is inefficient compared to the grain phase for typical physical conditions in protostellar environments (Geppert et al. 2006). Consequently, methanol is often used to signify the presence of thermally evaporated COMs in hot cores and hot corinos.

In the context of low-mass young stellar objects (YSOs), COMs were found in a few cases specifically associated with young stellar and protoplanetary disks. For example, methyl cyanide (CH<sub>3</sub>CN) and CH<sub>3</sub>OH were detected in the protoplanetary disks (Öberg et al. 2015; Walsh et al. 2016). Lee et al. (2017b) detected CH<sub>3</sub>OH, deuterated methanol (CH<sub>2</sub>DOH), methyl mercaptan (CH<sub>3</sub>SH), formamide (NH<sub>2</sub>CHO), and doubly deuterated formaldehyde (D<sub>2</sub>CO) in HH212. The distribution of these molecular emissions, above and below the dusty protoplanetary disk, is suggested to trace COMs formed in situ in the atmosphere of the disk. More recently, van't Hoff et al. (2018) detected methanol that appears to be thermally desorbed from grains in the disk of the young outbursting source V883 Ori.

Complex molecular species are mainly liberated from grain surfaces through thermal desorption with dust temperatures reaching ~85 K (Brown & Bolina 2007). Additional effects like photodissociation, reactive desorption, and energetic interaction may enhance gas-phase abundances of chemical species (e.g., Taquet et al. 2015; Sahu et al. 2018) including COMs (Drozdovskaya et al. 2015). For this reason, a few

<sup>&</sup>lt;sup>5</sup> Department of Physics and Astronomy, Graduate School of Science and Engineering, Kagoshima University, 1-21-35 Korimoto, Kagoshima 890-0065, Japan Received 2018 October 24; revised 2019 January 14; accepted 2019 January 16; published 2019 February 25

COMs have been seen in the peripheral region of protostellar envelopes (e.g., Jaber et al. 2014) and in shocks produced by fast jet and molecular outflow (e.g., Palau et al. 2017 and references therein).

Thanks to the advent of interferometric facilities like the Atacama Large Millimeter/submillimeter Array (ALMA), spectral signatures of COMs can be observed and mapped with high sensitivity and angular resolution at the subarcsecond level, differentiating their emission regions. Previously, interferometric observations of hot corinos (e.g., Bottinelli et al. 2004; Kuan et al. 2004; Bisschop et al. 2008; Jørgensen et al. 2011, 2016; Codella et al. 2016) unveiled the presence of several COMs and in some cases their distributions, too.

The IRAS 4A, one of the first known hot corino objects, is located in the Perseus molecular cloud at a distance of 235 pc (Hirota et al. 2008). A recent result from *Gaia* measured the distance to the Perseus molecular cloud to be  $293 \pm 22 \text{ pc}$ (Ortiz-León et al. 2018; Zucker et al. 2018), so we adopt this updated distance ( $\sim$ 293 pc) throughout the paper. The overall luminosity and envelope mass of the object are 9.1  $L_{\odot}$  and 5.6  $M_{\odot}$ , respectively (Kristensen et al. 2012; Karska et al. 2013). In the centimeter to millimeter continuum imaging measurements, IRAS 4A shows two compact emission cores and a clumpy extended structure, and IRAS 4A1 (A1 hereafter) is found to be brighter than IRAS 4A2 (A2 hereafter; Choi et al. 2010, 2011). A1 and A2, separated by 1.78 ( $\sim$ 527 au), are likely a pair in a class 0 protobinary system originating from the same parent cloud (Jennings et al. 1987; Sandell et al. 1991; Lay et al. 1995; Looney et al. 2000) and are reported to have similarly powerful bipolar outflows (Santangelo et al. 2015). The IRAS 4A region therefore encompasses circumstellar disks associated with compact cores and protostellar envelopes around the individual protostars and a common envelope shared by the binary (Choi et al. 2011). Taquet et al. (2015), through comparatively low angular resolution ( $\sim 2''$ ) observations that were unable to disentangle A1 and A2, found the presence of several COMs, for example CH<sub>3</sub>OH, HCOOCH<sub>3</sub>, CH<sub>3</sub>OCH<sub>3</sub>, HCOCH<sub>2</sub>OH, and C<sub>2</sub>H<sub>5</sub>OH, toward IRAS 4A as a whole. Recently, López-Sepulcre et al. (2017) studied the complex organics in IRAS 4A with ALMA and the Plateau de Bure Interferometer (PdBI) at a higher angular resolution  $(\sim 0.75)$  and resolved the emissions from the two cores, A1 and A2. They found a striking contrast between these two neighboring cores: while A2 showed hot corino activity with enriched COM emission (Persson et al. 2012), no sign of COMs was detected in A1. López-Sepulcre et al. (2017) suggest that either A1 does not host a hot corino, or alternatively A1 may host a hot corino with size  $\sim$ 15 au (after scaling the adopted distance to 293 pc), which is six times smaller than that of A2.

Keeping all this in mind, in this paper we present ALMA observations of the protostellar binary IRAS 4A with a high resolution of ~0."3 (or equivalently 88 au in linear scale). We detected emission signatures of methanol and its various isotopologues as well as CH<sub>3</sub>CHO in A2, while these species showed primarily absorption features toward A1. We suggest that we are seeing COMs in the "atmosphere" of A1, which itself is readily developing into a hot corino object with an optically thick dust continuum emission. We describe the observational setup in Section 2, detail the results in Section 3, and discuss the implications of these results in Section 4.

#### 2. Observations

The observations of IRAS 4A were carried out by ALMA under the project code 2015.1.00147.S. Three Execution Blocks (EBs) were conducted with the ALMA Band 7 receiver on 2016 July 23 and 24 and 2016 December 14. The number of antennas in the 12 M array for the three EBs were respectively 39, 42, and 43. The phase center of the observations was set at  $R.A.(J2000) = 03^d 29^m 10.50, decl.(J2000) = +31.13'31.5',$ and the total integration time on source was approximately 84 minutes. We deployed seven spectral windows, including one broadband window centered at 350.714 GHz whose bandwidth and spectral channel width are 1.875 GHz and 976 kHz, respectively. The latter, with standard online Hanning smoothing applied, corresponds to a velocity resolution of  $0.84 \text{ km s}^{-1}$ . This paper focuses on the data from the above broadband window, and more details about the full observational setup can be found in our forthcoming paper (Y.-N. Su, 2019, in preparation).

The data were first calibrated by the ALMA observatory through the data reduction pipeline within the Common Astronomy Software Application package (version 4.7, McMullin et al. 2007). We then generated both the 0.84 mm continuum and spectral visibilities by fitting and subtracting continuum emission in the visibility domain. We used a Briggs weighting with a robustness parameter of 0.5 to form the images. The resulting synthesized beam size is  $0\rlap.{''}30\times0\rlap.{''}20$  $(PA = -6^{\circ}.45)$  for the continuum map and is  $0''.31 \times 0''.20$  $(P.A = -24^{\circ})$  for the spectral data cubes (for a typical line transition only). We subsequently used MIRIAD (Sault et al. 1995) and CASSIS (developed by IRAP-UPS/CNRS, http:// cassis.irap.omp.eu) for further image inspection and spectral line analysis. The resulting rms level is  $\sim$ 8 and 3 mJy beam<sup>-</sup> in the continuum image and spectral cubes, respectively, with the noise rms being strongly limited by the imaging dynamical range in the continuum image, due to the presence of very bright features.

## 3. Results

## 3.1. Dust Continuum Emission

Figure 1(a) shows the 0.84 mm ( $\sim$ 357 GHz) continuum toward IRAS 4A. At an angular resolution of  $0.31 \times 0.20$ , IRAS 4A is clearly resolved into two components, with A1 located in the southeast and A2 in the northwest. A1 and A2 each appears to consist of a compact emission feature and an outer extended feature. We applied a two-component 2D Gaussian fitting to the two sources and summarize the fitting results in Table 1. Overall we recovered within the region a flux density of 7.24 Jy. Previous single dish observations by Smith et al. (2000) at 0.85 mm reported a peak flux density of 10.3 Jy beam<sup>-1</sup> within a 16" beam toward IRAS 4A. Sandell & Knee (2001), on the other hand, measured at 0.85 mm a peak flux density of 9.05 Jy toward the same direction. Considering calibration uncertainties, these results appear consistent and are about only 20% larger than our ALMA measurement. Given that the integrated region of single dish observations is also larger than the extent of the IRAS 4A centroid, we conclude that the missing flux issue, though it may result from the most extended envelope, is not severe and does not impact our science focusing on the compact continuum features.

The angular separation between A1 and A2 derived from the positions of the compact components listed in Table 1 is

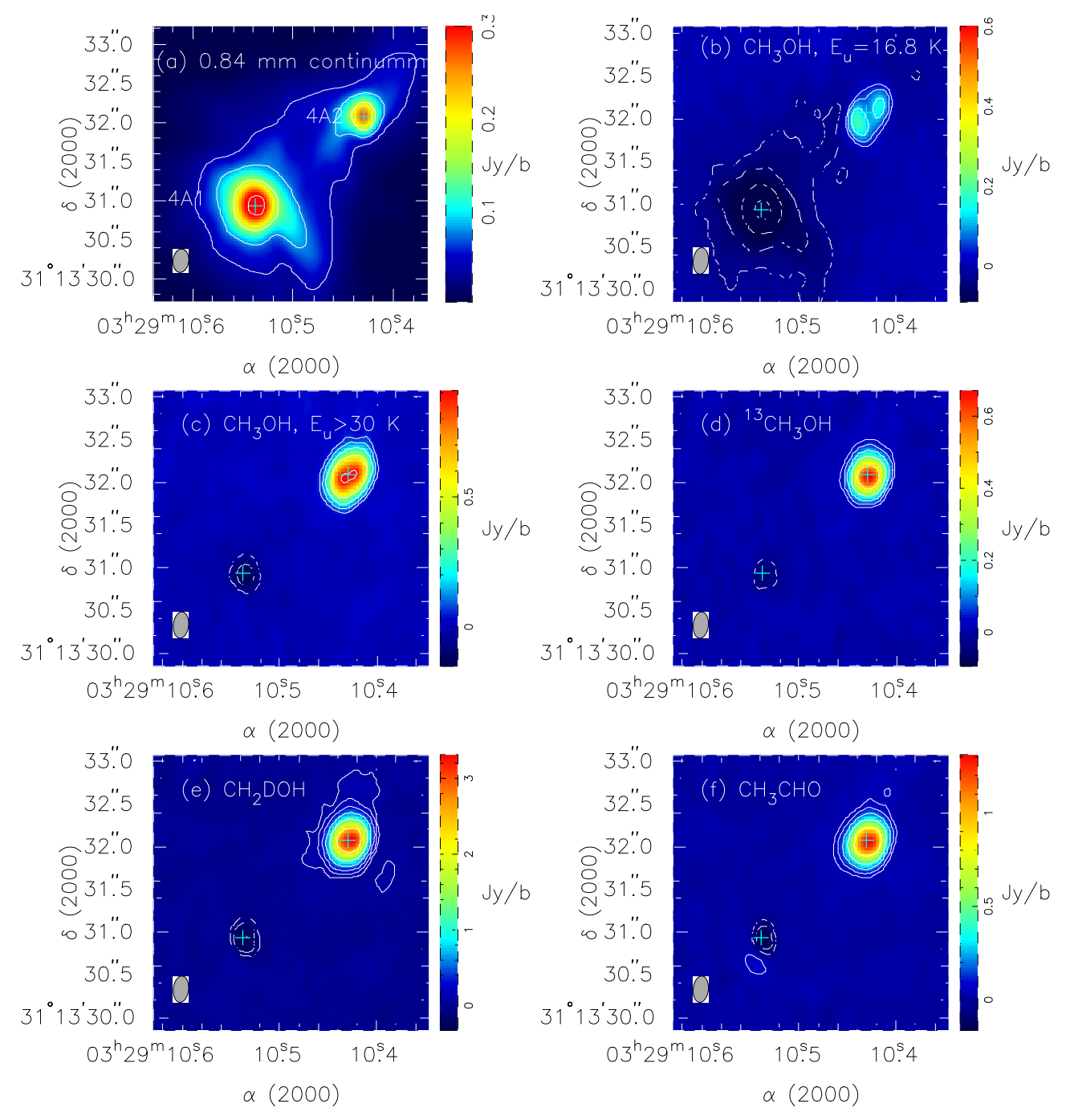


**Figure 1.** Integrated emission maps of IRAS 4A system for continuum (a) and different molecules (b–f) that are discussed in text. Panel (b) is for the  $1_{(1,1)}-0_{(0,0)++}$  transition, and panel (c) is for  $4_{(0,4)}-3_{(-1,3)}$  and  $9_{(5,5)}-10_{(4,6)}$  transitions of CH<sub>3</sub>OH. Panels (d)–(f) are for the molecules  $^{13}$ CH<sub>3</sub>OH, CH<sub>3</sub>CHO, and CH<sub>2</sub>DOH, respectively. For panels (d)–(f) we consider all of the transitions of the respective molecules that are detected in both A1 and A2. In the integrated maps, we have considered a total velocity interval of 2.4 km s<sup>-1</sup>. The contours are for  $5\sigma$ ,  $2\times5\sigma$ ,  $2\times10\sigma$ , ...., and  $-5\sigma$ ,  $2\times5\sigma$ ,  $2\times10\sigma$ , ...., with  $\sigma=8$ , 6, 11, 6, 15, 10 mJy km s<sup>-1</sup> for the images in panels (a)–(f), respectively.

1."8, in agreement with previous measurements (e.g., López-Sepulcre et al. 2017, and references therein). For both A1 and A2, the diameters of the compact component are equivalent to about 55–115 au, and the sizes of the extended envelope span about several hundreds to nearly 1000 au. The brightness temperatures derived from the observed peak continuum are 57 K and 42 K toward A1 and A2, respectively. The relatively high brightness temperatures readily indicate that the center positions of both A1 and A2 are very warm. We note that these

brightness temperatures are the beam-average values, and the actual brightness temperatures, depending on the source filling factor, could be further inflated.

Assuming a gas-to-dust ratio of 100, a (uniform) dust temperature of 60 K, a dust opacity  $\kappa_{\nu} = 0.006 \ (\nu/245 \ \text{GHz})^{\beta} \ \text{cm}^2 \ \text{g}^{-1}$  (Kramer et al. 1998; Shepherd & Watson 2002), an opacity index  $\beta = 1.5$ , and a distance of 293 pc to IRAS 4A, the dust and gas mass is estimated to be 0.15, 0.49, 0.07, and 0.50  $M_{\odot}$  for the 4A1 compact component, 4A1 extended component, 4A2

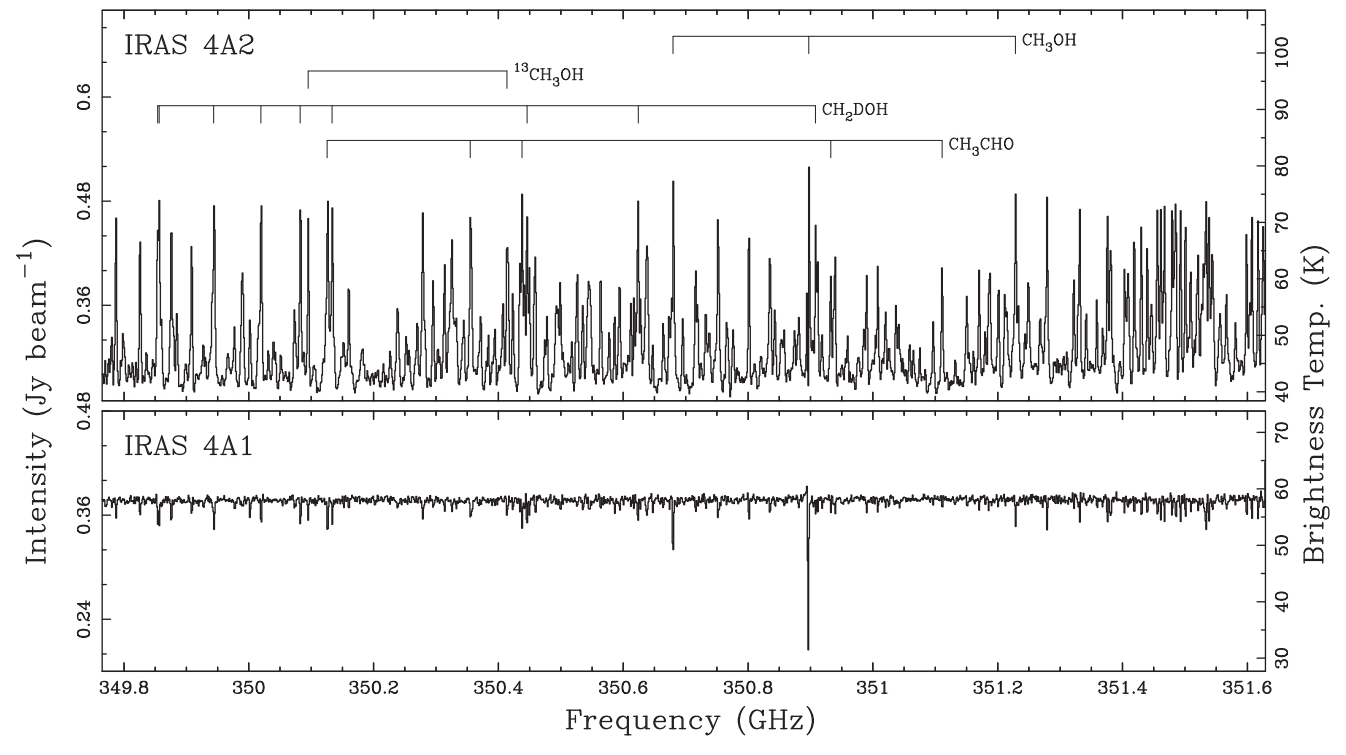


**Figure 2.** The upper panel shows spectral emission toward A2. Spectral transitions toward another core of IRAS 4A, A1, are detected in absorption (lower panel). Some of the identified transitions for the molecules CH<sub>3</sub>OH, <sup>13</sup>CH<sub>3</sub>OH, CH<sub>3</sub>CHO, and CH<sub>2</sub>DOH are marked. Along the *Y* axis we show real brightness temperature and intensity considering the continuum emission.

Table 1							
Parameters	of Continuum	Sources					

Source	Component	Position (I	Position (ICRS 2000)		Deconvolved Size			Mass
		$\alpha$	δ	$S_{\rm int}$ (mJy)	max"	min"	P.A.°	$M_{\odot}$
4A1	compact	03 29 10.538	+31 13 30.93	923	0.397	0.354	64.1	0.15
	extended	03 29 10.523	+31 13 30.69	2979	1.937	1.282	47.0	0.49
4A2	compact	03 29 10.430	+31 13 32.08	404	0.274	0.168	-82.2	0.07
	extended	03 29 10.448	+31 13 32.12	3035	2.973	1.167	-53.8	0.50

compact component, and 4A2 extended component, respectively; calculations are based on the optically thin assumption. Using the above-mentioned parameters, the  $\rm H_2$  column density toward the 4A1 centroid is estimated to be at least  $1.3 \times 10^{26}$  cm<sup>-2</sup>. Such a high molecular gas column density will lead to a visual extinction  $A_{\nu} > 100,000$ . Note that the estimated dust and gas mass of the 4A1 compact component is most likely a low limit given that there are indications of the A1 dust continuum being optically thick throughout the radio to submillimeter bands, as discussed in Section 4.1.

### 3.2. Detected Molecules and Their Distribution

In Figure 2 we display the spectra toward the continuum A1 and A2 peaks over the full 1.875 GHz spectral window centered at 350.714 GHz. Line features from methanol (CH<sub>3</sub>OH) and its isotopologues (<sup>13</sup>CH<sub>3</sub>OH and CH<sub>2</sub>DOH), as well as those from acetaldehyde (CH<sub>3</sub>CHO), as identified and discussed below, are marked in Figure 2 and listed in more detail in Table 2.

Toward A1, the spectrum throughout the window exhibits rich and almost exclusively absorption features, regardless of their excitation temperatures. This is complementary evidence suggesting that the continuum dust emission along the A1 line of sight is optically thick. In contrast, the spectrum toward A2

shows a multitude of emission lines. Many spectral features (e.g., CH<sub>3</sub>OH) from A2 display noticeably similar peak intensities at around 75 K, indicative of a "saturated" and thus optically thick nature of those respective lines.

In this paper, we focus on the detection and analysis of CH<sub>3</sub>OH, its isotopologues including <sup>13</sup>CH<sub>3</sub>OH and CH<sub>2</sub>DOH, and CH<sub>3</sub>CHO in both the A1 and A2 cores of IRAS 4A. As noted, CH<sub>3</sub>OH is a robust tracer for highlighting surface chemistry that occurs within interstellar ices on the grain surface. To firmly secure the spectral identification, we examined the spectral features that bear strong (emission/ absorption) intensities and are relatively well separated from line confusion/contamination. We visualized the spectral data in CASSIS for initial line identifications. Assuming a systematic velocity of 6.96 km s<sup>-1</sup> (Di Francesco et al. 2001) and employing the JPL (Pickett et al. 1998) and CDMS (Müller et al. 2001, 2005) databases, we generated synthetic spectra within CASSIS. Essentially all isolated transitions from these molecules with their Einstein coefficient  $A_{ii} \ge 10^{-5}$  are well matched (at a level of  $3\sigma$  and above), while those with  $A_{ij} < 10^{-5}$  are likely below our detection threshold or are blended by nearby stronger features from other species. CH<sub>3</sub>OH transitions are most intense, and there is negligible

Table 2 Molecular Transitions Detected toward IRAS 4A

Molecule	Transition <sup>a</sup>	$\nu_0$ (MHz)	$E_{\rm up}$ (K)	$A_{ij} \text{ s}^{-1}$	Intensity(K)	$V_{\rm lsr}~({\rm km~s}^{-1})$	$\Delta V$	Intensity(K)	$V_{\rm lsr}~({\rm km~s}^{-1})$	$\Delta V$
					Trans	sitions toward IRAS	4A2	Transit	ions toward IRAS	4A1 <sup>b</sup>
CH <sub>3</sub> OH	$vt = 0 \ 4(0,4)-3(-1,3)$	350687.73	36.33	8.67E-5	$31.05 \pm 3.06$	$6.30 \pm 0.13$	$1.93 \pm 0.25$	$-7.69 \pm 0.80$	$7.03 \pm 0.08$	$1.25 \pm 0.16$
CH <sub>3</sub> OH	$vt = 0 \ 1(1,1) - 0(0,0) + +$	350905.12	16.84	3.31E-4	$38.49 \pm 2.72$	$6.59 \pm 0.10$	$2.06 \pm 0.12$	$-20.59 \pm 5.95$	$7.10 \pm 0.24$	$1.18 \pm 0.38$
CH <sub>3</sub> OH	$vt = 0 \ 9(5,5) - 10(4,6)$	351236.34	240.51	3.66E-5	$27.76 \pm 1.47$	$6.49 \pm 0.07$	$2.09\pm0.14$	$-3.00 \pm 0.15$	$6.64\pm0.03$	$0.96\pm0.06$
<sup>13</sup> CH <sub>3</sub> OH	$vt = 0 \ 1(1,0) - 0(0,0) + +$	350103.12	16.80	3.29E-4	$25.59 \pm 0.86$	$6.65 \pm 0.03$	$1.49 \pm 0.06$	$-2.19 \pm 0.17$	$7.01 \pm 0.05$	$1.06 \pm 0.10$
<sup>13</sup> CH <sub>3</sub> OH	$vt = 0 \ 8(1,7) - 7(2,5)$	350421.58	102.62	7.03E-5	$22.91\pm4.58$	$6.53 \pm 0.29$	$1.60\pm0.66$	$-1.52 \pm 0.18$	$6.58\pm0.08$	$1.13\pm0.18$
CH <sub>2</sub> DOH	8(4,4)–8(3,6) e <sub>1</sub>	349864.35	149.21	1.07E-4	$28.33 \pm 1.06$	$6.65 \pm 0.09$	$1.54 \pm 0.14$	$-1.84 \pm 0.29$	$6.76 \pm 0.12$	$1.05 \pm 0.29$
CH <sub>2</sub> DOH	8(4,5)-8(3,5) e <sub>1</sub>	349862.11	149.21	1.07E-4	$25.23 \pm 0.13$	$7.00 \pm 0.02$	$1.65 \pm 0.02$	$-2.60 \pm 0.41$	$6.82 \pm 0.16$	$1.02 \pm 0.21$
CH <sub>2</sub> DOH	$7(4,4)-7(3,4) e_1^c$	349951.68	132.07	1.00E-4	$30.93 \pm 1.29$	$6.15 \pm 0.06$	$2.14 \pm 0.13$	$-2.69 \pm 0.43$	$6.60 \pm 0.14$	$1.29 \pm 0.24$
CH <sub>2</sub> DOH	$6(4,3)-6(3,3)$ $e_1^d$	350027.35	117.08	9.06E-5	$30.86 \pm 0.87$	$6.38 \pm 0.03$	$1.86 \pm 0.07$	$-3.10 \pm 0.43$	$6.61 \pm 0.08$	$1.01 \pm 0.18$
CH <sub>2</sub> DOH	$5(4,2)-5(3,2) e_1^e$	350090.24	104.23	7.58E-5	$30.10 \pm 1.29$	$6.38 \pm 0.05$	$1.83 \pm 0.10$	$-2.25 \pm 0.14$	$6.61 \pm 0.06$	$1.33 \pm 0.10$
CH <sub>2</sub> DOH	$4(4,1)-4(3,1) e_1^f$	350141.30	93.53	5.03E-5	$26.73 \pm 2.16$	$6.38 \pm 0.11$	$2.16 \pm 0.21$	$-2.25 \pm 0.26$	$6.60 \pm 0.09$	$1.20 \pm 0.16$
CH <sub>2</sub> DOH	6(2,5)-5(1,5) e <sub>1</sub>	350453.86	71.55	1.39E-4	$27.29 \pm 1.35$	$6.79 \pm 0.06$	$1.75 \pm 0.11$	$-2.23 \pm 0.08$	$7.02 \pm 0.03$	$1.06 \pm 0.04$
$CH_2DOH$	5(1,4)-5(0,5) e <sub>1</sub>	350632.07	48.98	2.07E-4	$28.98 \pm 2.07$	$7.05\pm0.09$	$1.90 \pm 0.19$	$-2.39 \pm 0.30$	$7.30\pm0.10$	$1.18\pm0.17$
CH <sub>3</sub> CHO	$v = 0.18(3,15) - 17(3,14) E^{d}$	350133.42	179.2	1.44E-3	$28.17 \pm 3.12$	$6.03 \pm 0.22$	$2.30 \pm 0.45$	$-3.58 \pm 0.31$	$6.30 \pm 0.06$	$1.18 \pm 0.13$
CH <sub>3</sub> CHO	v = 0.18(1,17) - 17(1,16) E	350362.84	163.46	1.47E-3	$26.16 \pm 1.28$	$6.21 \pm 0.08$	$2.23 \pm 0.17$	$-1.84 \pm 0.19$	$6.36 \pm 0.11$	$1.60 \pm 0.20$
CH <sub>3</sub> CHO	v = 0.18(1,17) - 17(1,16) E	350445.78	163.42	1.47E-3	$26.51 \pm 2.02$	$6.66 \pm 0.10$	$2.00\pm0.20$	$-2.70 \pm 0.04$	$6.96 \pm 0.01$	$1.23\pm0.02$
CH <sub>3</sub> CHO	18(3,15)3-17(3,14)3	350940.56	383.69	1.45E-3	$15.15 \pm 0.71$	$6.79 \pm 0.05$	$1.63 \pm 0.09$			
CH <sub>3</sub> CHO	18(1,17)5-17(1,16)5	351118.83	368.32	1.45E-3	$16.04 \pm 0.43$	$6.71 \pm 0.03$	$1.60 \pm 0.06$	•••		

#### Notes.

<sup>&</sup>lt;sup>a</sup> Transitions are in the form  $N(K_a, K_b) p v$  and  $N(K_a, K_b) v$ .

<sup>b</sup> The values of intensities are negative as transitions are detected in absorption.

<sup>&</sup>lt;sup>c</sup> Four transitions.

d Two transitions.

<sup>&</sup>lt;sup>e</sup> Two transitions.

f Two transitions.

contamination from other molecular species. All CH<sub>3</sub>OH transitions falling in the spectral coverage are identified, as listed in Table 2. In particular, the transitions 1(1,1)–0(0,0)++ to the ground state are prominently detected with a deep absorption feature toward A1 and an inverse P Cygni profile toward A2. Though CH<sub>2</sub>DOH molecular transitions are detected without confusion, some of its transitions are blended themselves. For example, two CH<sub>2</sub>DOH transitions (8<sub>(4,4)</sub> – 8<sub>(3,6)</sub> e1 and 8<sub>(4,5)</sub> – 8<sub>(3,5)</sub> e1), with similar excitation energies  $E_u$  and frequencies, overlap at around 349.864 GHz. The detected molecular transitions of the selected species are common toward both cores, except that the molecular transitions with  $E_u$  > 240.5 K of CH<sub>3</sub>CHO were not detected toward A1.

We applied Gaussian profile fitting to extract the spectral parameters of the identified features. We list the fitting results in Table 2 and plot the profiles in Figures 3 and 4. During the fitting process, we consider the velocity range carefully to fit the spectral profile. In some cases, we excluded some channels to avoid line contamination and other kinematic features (e.g., inverse P Cygni, see Figure 5). The fitting results of spectral profiles from different transitions of a molecule have peaks around a common local standard of rest velocity, considering the uncertainties of measurements. The averaged velocity of the emission features (excluding the inverse P Cygni profile) toward A2 is 6.6 km s<sup>-1</sup>. Given the limited velocity resolution, this velocity is consistent with the gas velocity seen in previous works (e.g., average value 6.8 km s<sup>-1</sup>, López-Sepulcre et al. 2017). The averaged velocity of absorption features toward A1 is 6.8 km s<sup>-1</sup>. Meanwhile, there does not appear to be any trend of velocity variation among the transitions of different excitation energy. When this is compared with the systemic velocity of 6.7 km  $s^{-1}$  adopted by Choi et al. (2007), there is no clear indication of (infall) motion in the absorbing gas. Based on the profile fitting (Table 2), we also note that the line width  $\Delta V$ s are  $\sim 1.0$ –1.5 km s<sup>-1</sup> for the (absorption) features in A1, while  $\Delta V$ s are  $\sim 1.5-2.3$  km s<sup>-1</sup> for the (emission) lines in the A2 core.

Figures 1(b)-(f) show the velocity integrated intensity maps of the molecules described in the text. In all panels, dashed contours in the map represent absorption, and solid contours represent emission. Three CH<sub>3</sub>OH transitions are detected in both A1 and A2. We plotted the integrated emission of the low-temperature  $E_{\mu} = 16.8$  K transition and the remaining two transitions (see Table 2) separately in Figures 1(b) and (c). From the two panels, we see that the absorption feature associated with the CH<sub>3</sub>OH 1 (1,1)-0(0,0)++ line  $(E_u = 16.8 \text{ K})$  around the A1 core is extended and has a size of  $0.87 \times 0.74$  (deconvolved from the beam after 2D Gaussian fittings), reflecting its low-lying energy nature. The integrated emission for the same transition toward A2 is also affected by the absorption part of the inverse P Cygni profile. The absorption around the A1 core for the two other higher  $E_{\mu}$  methanol transitions have a compact size of 0."42  $\times$  0."29. To enhance the imaging quality, for species other than CH<sub>3</sub>OH, the integrated intensity maps are made by stacking the detected transitions all together. Based on the 2D Gaussian fitting, we find that the absorption features for <sup>13</sup>CH<sub>3</sub>OH, CH<sub>3</sub>CHO, and CH<sub>2</sub>DOH around the A1 core are all compact.

#### 3.3. Gas Temperatures and Column Densities

Toward IRAS 4A2, there are a large number of emission lines showing noticeably similar intensity levels at around 70 K (without continuum subtraction), as shown in Figure 2. This is particularly true for the three detected  $CH_3OH$  transitions, all of the  $CH_2DOH$  transitions, and at least the three low-energy  $CH_3CHO$  transitions, as also shown in Figure 3. Given that these emission features originate from different species with different excitation energies and Einstein A coefficients, their common brightness can be understood only if all of these lines are optically thick and saturated. The opaque nature indicates that the molecular gas at A2 is at least as hot as 70 K at its "surface." For  $^{13}CH_3OH$  in A2, the emissions may be optically thin, although the high  $E_u$  line is possibly blended by an interloper. Additionally, a couple of high  $E_u$   $CH_3CHO$  transitions do not seem to be saturated.

For these cases where we have detected multiple optically thin transitions from the same molecule, we may estimate the gas temperature using the rotation diagram method (Turner 1991; Herbst & van Dishoeck 2009 and references therein). Following the standard radiative transfer equation, we have

$$I_{\nu} = J_{\nu}(T_{\rm ex})(1 - e^{-\tau_0}) + J_{\nu}(T_{\rm bg})e^{-\tau_0}$$
 (2)

where  $I_{\nu}$  is the observed brightness at the line frequency  $\nu$ ,  $J_{\nu}$  is the source function  $(=(h\nu/k)[\exp(h\nu/kT)-1]^{-1}$ ,  $T_{\rm ex}$  and  $T_{\rm bg}$  are the gas excitation temperature at that transition and the background brightness temperature, respectively, and  $\tau_0$  is the optical depth at the line center. Equivalently,

$$I_{\nu} = J_{\nu}(T_{\text{ex}}) + (J_{\nu}(T_{\text{bg}}) - J_{\nu}(T_{\text{ex}}))e^{-\tau_0}.$$
 (3)

The observed continuum-subtracted line brightness temperature  $\Delta T_B$  can be expressed as

$$\Delta T_{\rm B} = I_{\nu} - J_{\nu}(T_{\rm bg}) \tag{4}$$

$$= [J_{\nu}(T_{\rm ex}) - J_{\nu}(T_{\rm bg})(1 - e^{-\tau_0}). \tag{5}$$

Equation (4) is the same as Equation (A1) of Turner (1991). When the line emission is assumed to be optically thin, the upper-level population  $N_u$  is given by Equation (A3) of Turner (1991):

$$\frac{N_u}{g_u} = \frac{T_{\rm ex}}{T_{\rm ex} - T_{\rm bs}} \frac{3kW}{8\pi^3 \nu S \mu^2}$$
 (6)

where  $g_u$  is the degeneracy of the upper level, k is the Boltzmann constant, S is the line strength,  $\mu$  is the dipole moment,  $W = \int \Delta T_{\rm B} dv$  is the integrated line intensity in K km s<sup>-1</sup>, and the Rayleigh–Jeans approximation has been applied. Furthermore, the level population can be described using a Boltzmann distribution, characterized by a single (rotation) temperature  $T_{\rm ex} = T_{\rm rot}$ , if its excitation is assumed to be in local thermodynamic equilibrium (LTE). The total molecular column density and the excitation (rotation) temperature can thus be related by the relation

$$\frac{N_u}{g_u} = \frac{N_{\text{tot}}}{Q_{\text{tot}}} e^{-E_u/KT_{\text{rot}}} \tag{7}$$

where  $N_{\text{tot}}$  is the total column density, and  $Q_{\text{tot}}$  is the rotational partition function at  $T_{\text{rot}}$ . Combining Equations (5) and (6), we

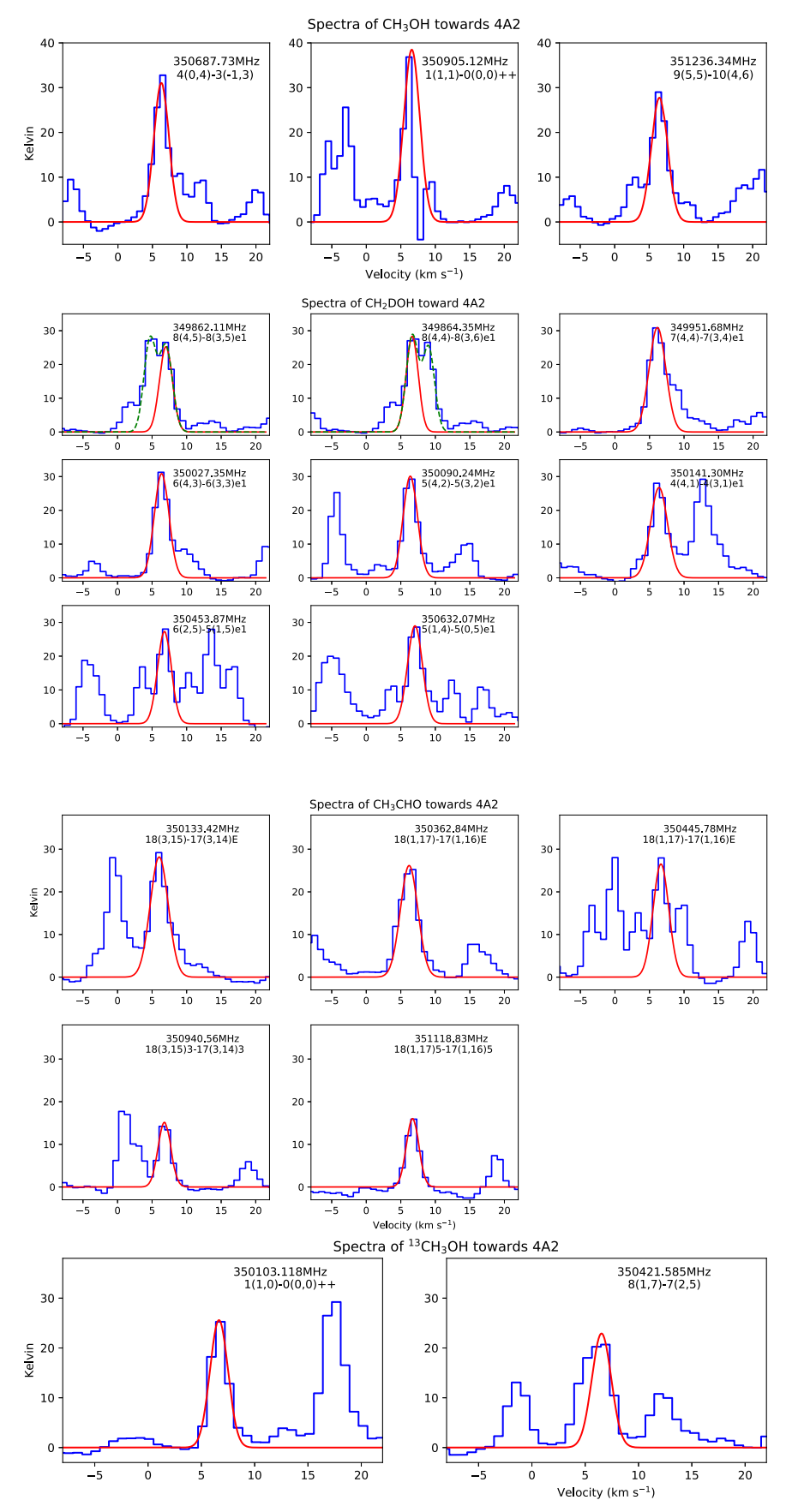


Figure 3. Spectra of 18 lines (blue) are detected toward IRAS 4A2. Gaussian fitting of the spectra are shown in red, and results of the fittings are given in Table 2. Here we show the continuum-subtracted intensity of the spectra.

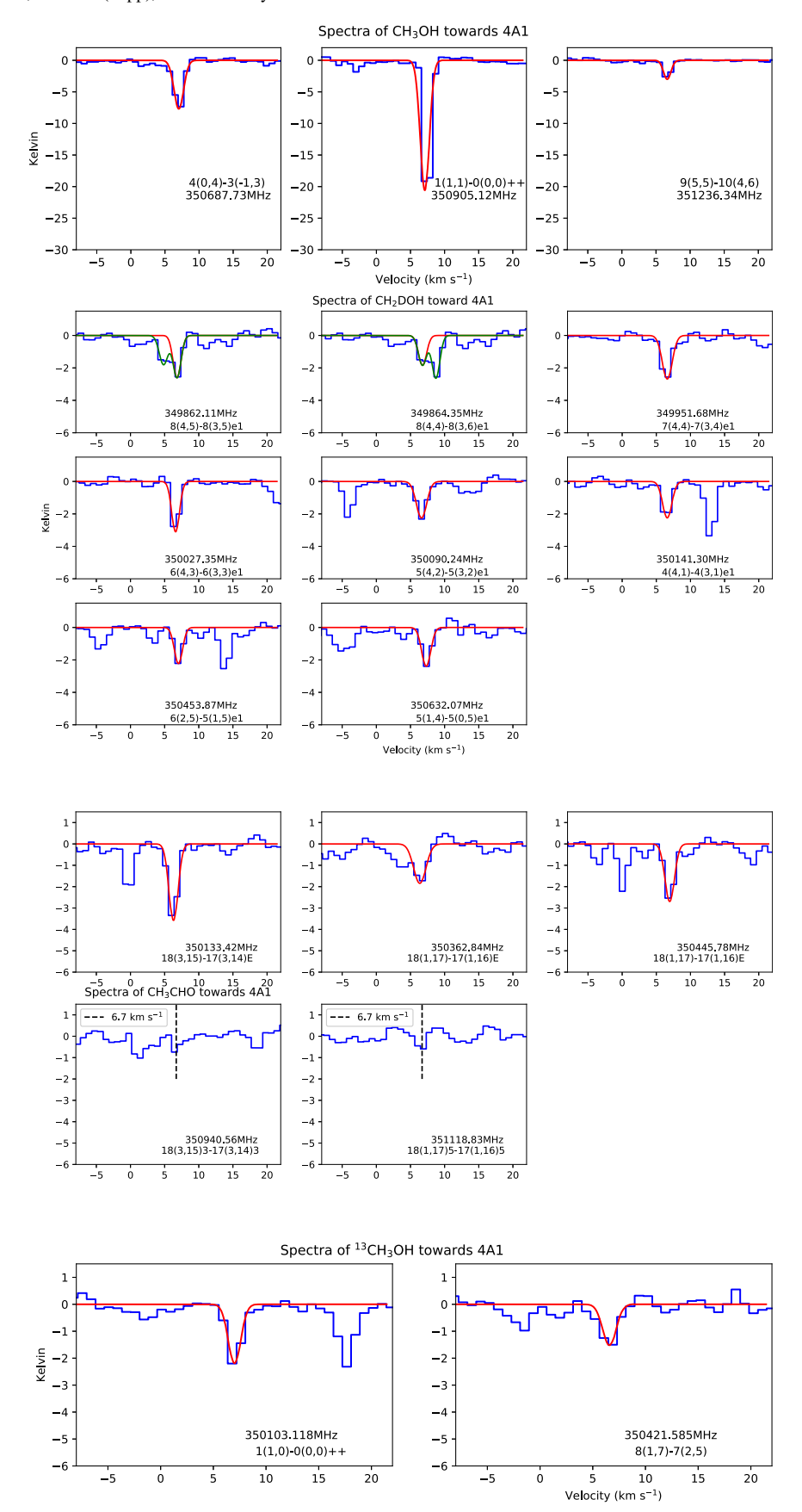
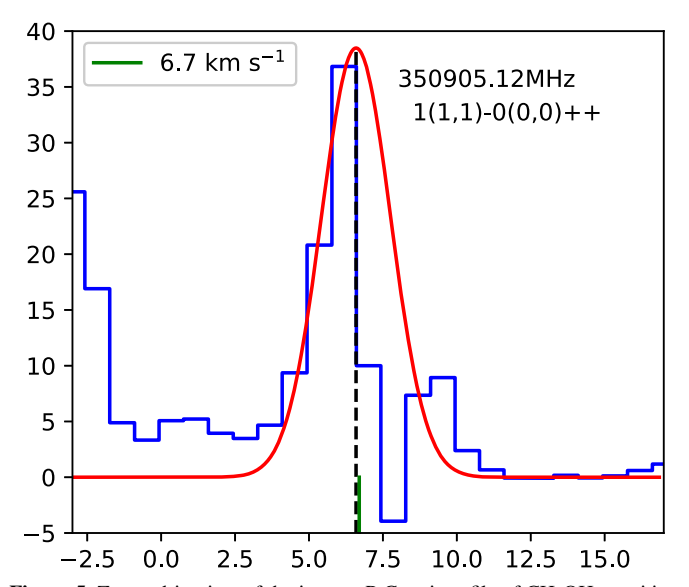


Figure 4. Spectra of 16 lines (blue) are detected in absorption toward IRAS 4A1. Gaussian fitting of the spectra are shown in red, and results of the fittings are given in Table 2. Here we show the continuum-subtracted intensity of the spectra.



**Figure 5.** Zoomed-in view of the inverse P Cygni profile of  $CH_3OH$  transition toward A2. The dotted line represents the peak velocity of Gaussian fitting, assuming the systematic velocity is 6.7 km s<sup>-1</sup>.

can find

$$\log \frac{3kW}{8\pi^3 \nu S \mu^2} = \log \frac{N_{\text{tot}}}{Q_{\text{tot}}} - \frac{E_u}{k} \frac{1}{T_{\text{rot}}} - \log \frac{T_{\text{rot}}}{T_{\text{rot}} - T_{\text{bg}}}.$$
 (8)

This equation, with a negligible  $T_{\rm bg}$ , and hence a negligible last term, forms the conventional rotation diagram. That is, for the same molecule with multiple detected transitions, one can plot  $\log(N_u/g_u)$  versus  $E_u$  and determine  $T_{\rm rot}$  and  $N_{\rm tot}$ . We note that, though, when  $T_{\rm bg}$  cannot be fully neglected but the line opacity remains reasonably small (<1), the plot of  $\log(N_u/g_u)$  versus  $E_u$  still gives rise to a slope of 1/k  $T_{\rm rot}$ .

We applied the rotation diagram method to the  $^{13}\text{CH}_3\text{OH}$  and CH<sub>3</sub>CHO transitions detected toward A2. As shown in Figure 6, we obtained rotation temperatures of 375.13  $\pm$  270.02 K and 261.31  $\pm$  10.79 K for  $^{13}\text{CH}_3\text{OH}$  and the CH<sub>3</sub>CHO, respectively. These temperatures should be taken as upper limits though, as their corresponding lower  $E_u$  lines are possibly optically thick. Goldsmith & Langer (1999) pointed out that, when the optical depth is not negligible, the true total column density  $N_{\text{tot}}$  is related to the column density under the optically thin condition  $N_{\text{tot}}^{\text{thin}}$  by the following relation:

$$N_{\text{tot}} = N_{\text{tot}}^{\text{thin}} \frac{\tau}{1 - \exp(-\tau)}.$$
 (9)

That is, when the low  $E_u$  lines are optically thick, their respective  $N_u$  need to be corrected upward, leading to a steeper slope in the rotation diagram and hence a lower rotation temperature. We also obtained lower limits on their column densities. Indirectly we can have an educated guess for the CH<sub>3</sub>OH column density also by considering the isotopic ratio  $^{12}\text{C}/^{13}\text{C} \sim 70$  (Sheffer et al. 2007).

The situation toward IRAS 4A1, for its exclusively absorption features, can be more complicated. As the absorption features have various depths, in a naive scenario (Scenario I, see Figure 7), we assume that most, if not all, of the observed transitions in A1 are optically thin and there is no saturation in absorption. We regard the continuum emission as the

"background" radiation in the radiative transfer equation, and the absorbing molecular line forms in a "foreground" layer. We would therefore have both  $(T_{\rm ex}-T_{\rm bg})$  and W terms in Equation (5) negative as  $T_{\rm ex} < T_{\rm bg}$  and  $\Delta T_B < 0$  and proceed with the rotation diagram method.

When this Scenario I is applied to the CH<sub>3</sub>OH and  $^{13}$ CH<sub>3</sub>OH transitions in A1, we obtain Figure 6, which indicates that the corresponding rotation temperatures for CH<sub>3</sub>OH and  $^{13}$ CH<sub>3</sub>OH are  $140.39 \pm 6.63$  K and  $58.94 \pm 3.74$  K, respectively. However, CH<sub>2</sub>DOH does not fit with a well-defined rotational temperature, probably due to line blending. The detected transitions of CH<sub>3</sub>CHO toward A1 may be optically thin, but they have very closely spaced  $E_u$  values ( $\sim 163-179$  K) and do not provide good constraints on the temperature through a rotation diagram. The column densities are shown in Table 3. For molecules where we do not have any estimation of rotational temperature, we choose the temperature to be 200 K and calculated the column densities by averaging the results from all of the detected transitions of a molecule.

## 4. Discussion

While the observed forest of emission line features of COMs supports the hot corino nature of IRAS 4A2, as was established by previous studies (e.g., Santangelo et al. 2015; Taquet et al. 2015; López-Sepulcre et al. 2017), the nature of A1 is much less clear. Taquet et al. (2015) made detailed studies of COMs in selected low-mass YSOs, including NGC 1333 IRAS 4A. Even though the angular resolution of their observations only marginally resolved A1 and A2, it was clear that A1 is devoid of COM emission features. A lack of COM emission lines toward A1 was noticed by Santangelo et al. (2015) in their study of the bipolar outflows associated with IRAS 4A. Based on the velocities and extents of the bipolar outflows, Santangelo et al. (2015) proposed a younger dynamical age of A1 as compared to A2. Using observations with PdBI and ALMA, López-Sepulcre et al. (2017) further reaffirmed a significant contrast of COM features between A1 and A2. López-Sepulcre et al. (2017) detected no COM emission but marginal absorption features of CH<sub>3</sub>CHO, HCOOCH<sub>3</sub>, and (CH<sub>3</sub>)<sub>2</sub>CO toward A1 and attribute these features to either an opaque absorbing foreground or a very small and severely beam-diluted emission region. In particular, they estimated that the size of the emitting region should be of order 15 au (after scaling the adopted distance to 293 pc) or smaller if it is not obscured by the foreground dust.

# 4.1. Continuum Opacity

In contrast to previous presumptions, we present below several lines of evidence that point to the A1 continuum emission from centimeter to submillimeter wavelengths being optically thick. First of all, the rich absorption lines in combination with the absence of the emission feature we observed at 0.84 mm is an indication of either A1 being genuinely deficient in trace molecular species or the continuum being optically thick and attenuating the embedded molecular emissions.

Second, as presented in Section 3.1, the brightness temperature of the compact component toward A1 is nearly 60 K at an angular resolution of 0.73 by 0.72. At 1.2 mm (250 GHz), López-Sepulcre et al. (2017) detected with ALMA a peak continuum flux of 542 mJy toward the A1 centroid at an

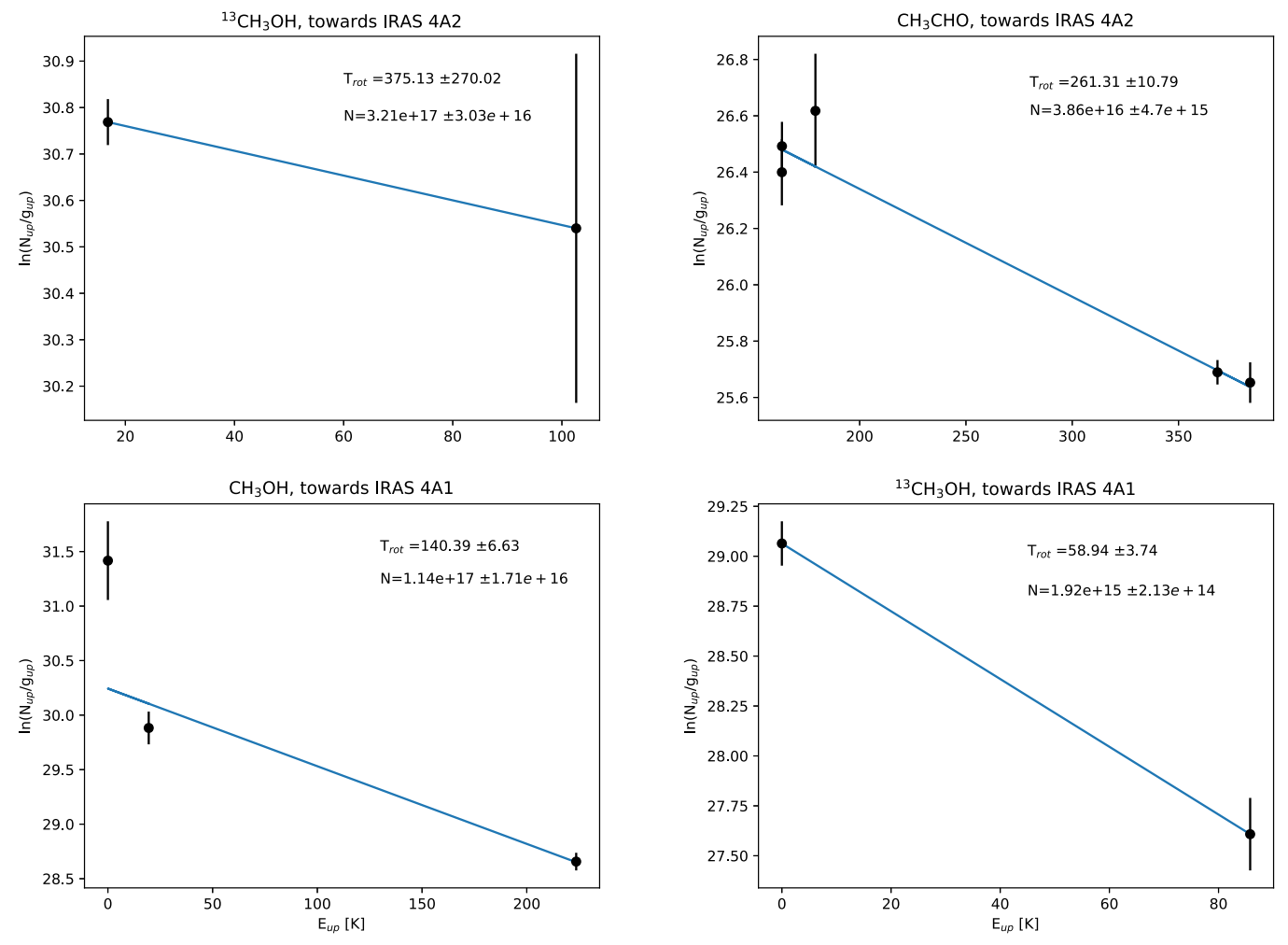


Figure 6. Rotational diagram of <sup>13</sup>CH<sub>3</sub>OH and CH<sub>3</sub>CHO toward IRAS 4A2 and <sup>13</sup>CH<sub>3</sub>OH and CH<sub>3</sub>OH toward IRAS 4A1. The best-fit values of rotational temperature and column density are mentioned in the panels.

angular resolution of 0."66 by 0."35. This leads to a brightness temperature of 46 K. With the Karl G. Jansky Very Large Array (JVLA) 6.9 mm observations at a resolution of  $0.49 \times 0.49$ , Liu et al. (2016) also reported a fairly high brightness temperature of 41 K toward A1. Recently VLA observations for the VLA Nascent Disk and Multiplicity (VANDAM) survey measured peak continuum fluxes of 4.151 mJy and 2.759 mJy at 8.1 mm and 10.3 mm, respectively, toward A1 (Cox et al. 2015). With their synthesized beam sizes of 0"224 by 0"199 and 0"25 by 0"25, these flux densities correspond to a brightness temperature of 83 K at 8.1 mm and 64 K at 10.3 mm. Given dust opacity is more optically thin at longer wavelengths, that is, scaling as  $\nu^{\beta}$  with  $\beta \sim 1.0$  or higher, one would expect that, at similar angular resolutions, the continuum brightness temperature measured at a lower frequency will be significantly weaker than that observed at a higher frequency. The beam dilution effect could further make the brightness lower if the low-frequency observations were done at a coarser angular resolution. We, for example, smooth our ALMA 0.84 mm continuum to have the same beam size as that of the JVLA 6.9 mm observations and find the resulting A1 peak brightness is 39 K, almost identical to the JVLA 6.9 mm measurement. With observations of these bands considered, the above-mentioned comparable brightness from 10 mm to 0.84 mm therefore implies an

opaque continuum emission throughout these bands toward the A1 peak, and the dusty opaque zone could be as large as the JVLA beam area of  $0.^{\prime\prime}49 \times 0.^{\prime\prime}40$ . In fact, a possible opaque nature of the 1.2 mm continuum emission of A1 was considered by López-Sepulcre et al. (2017), although it was ruled to be unlikely by the authors because of its corresponding large volume density of  $10^{11}$  cm<sup>-3</sup> toward the region. Meanwhile, in a spectral energy distribution (SED) modeling and analysis, Li et al. (2017) considered a two-component (disk +envelope) fitting, which results in a good representation of the measured SED data points and hinted at the A1 continuum being optically thick even down to centimeter wavelengths.

The possibility of A1 being optically thick throughout the centimeter to submillimeter bands has notable implications. All of the column densities and masses reported by previous studies should then only be considered as lower limits, as they were derived with the optically thin assumption. The lack of an emission spectral feature and hence the deficiency in trace (COM) species, compared to that of A2, should also be reconsidered, as their emission could be naturally blanked by the optically thick continuum. Additionally, the weak NH<sub>3</sub> line emission observed by Choi et al. (2007, 2011) toward A1 could also be partially understood if the continuum opacity remains substantial at 1.3 cm.

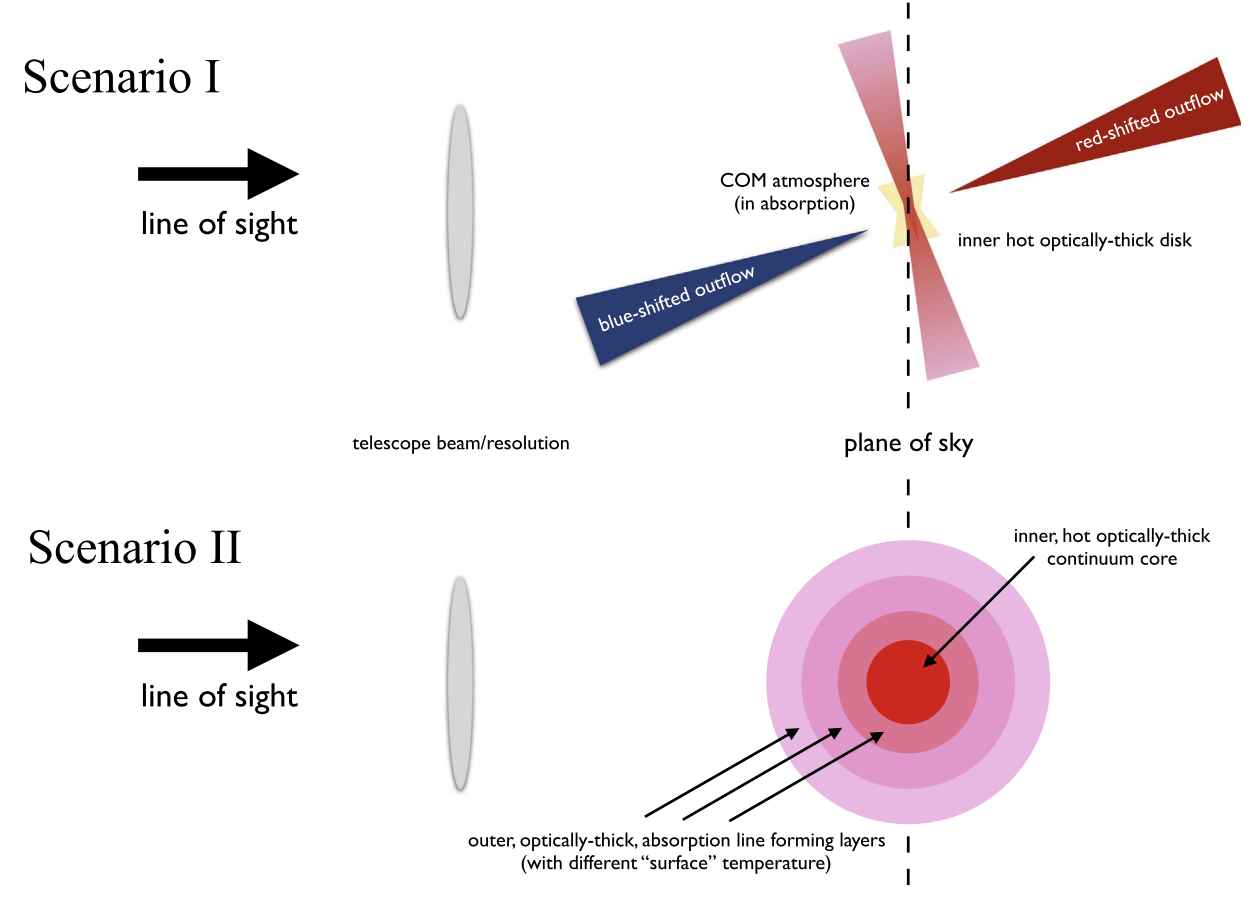


Figure 7. Schematic diagram for NGC 1333 IRAS 4A1 configuration.

In the case of A2, Liu et al. (2016) reported a much weaker brightness of  $\sim$ 2 K at 6.9 mm, about a factor of 20 lower than our ALMA 0.84 mm results. Note that the 0.84 mm brightness temperature smoothed to the JVLA 6.9 mm beam size is still as high as 23 K. The brightness difference indicates that the 6.9 mm continuum toward the A2 peak is likely optically thin.

# 4.2. COM Features

We have detected spectral features of CH<sub>3</sub>OH, CH<sub>2</sub>DOH, <sup>13</sup>CH<sub>3</sub>OH, and CH<sub>3</sub>CHO in both A1 and A2 of IRAS 4A. Toward A2, all features from these species, except CH<sub>3</sub>OH 1 (1,1)–0(0,0)++, are in emission. Many of the transitions are, as demonstrated in Section 3.2, optically thick with a brightness temperature of 70 K, suggesting that the gas is warm. The CH<sub>3</sub>OH 1(1,1)–0(0,0)++ line shows an inverse P Cygni profile, indicative of gas infall motion, and this will be discussed in a separate paper. Toward A1, our observations demonstrate conclusively, for the first time, absorption features from the selected COMs against the optically thick dust continuum emission.

Could both the absorption features toward A1 and the emission features toward A2 have a common, possibly foreground, origin? Yıldız et al. (2013) suggested tentatively a foreground layer of gas based on O<sub>2</sub> observations with the *Herschel Space Observatory* toward IRAS 4A, and this component has been incorporated for optimizing the model fitting of H<sub>2</sub>O spectra observed also with *Herschel* by Mottram et al. (2013) in IRAS 4A. This foreground cloud with an estimated velocity at around 8.0 km s<sup>-1</sup> also seems to be

present in the <sup>13</sup>CO (2-1) spectrum reported by Jørgensen et al. (2007, their Figure 6) in the PROSAC survey. However, this velocity component is 0.8–1.0 km s<sup>-1</sup> offset from the systemic velocity of IRAS 4A and is incompatible with our observed COM velocities. In addition, the spectral features of these COMs along the two close lines of sight (toward A1 and A2) have disparate velocities, line widths, and optical depths, strongly ruling out a common (foreground) origin of the observed COM absorption and emission.

Given that COMs have been observed sometimes in shocks associated with outflows (Sugimura et al. 2011), there is the possibility that the COM features are associated with the outflows in IRAS 4A. Santangelo et al. (2015) found a highvelocity jet from A1, while A2 drives a slower precessing jet, with both outflows primarily aligned along the north-south direction. On the other hand, our observed absorption and emission COM features trace rather closely the bright dust continuum. Furthermore, the observed line widths of the COM features toward the A1 and A2 continuum are relatively narrow, in contrast to the high outflow velocities of several tens of km s<sup>-1</sup> relative to the ambient in this region (Santangelo et al. 2015). An outflow origin of the COM features toward A1 and A2 is therefore unlikely, leaving the observed COMs most probably associated directly with the individual A1 and A2 continuum sources at  $\lesssim$ 0".3 or  $\lesssim$ 88 au scale.

As shown in Figure 1, the low  $E_u$  ( $\sim$ 16 K) CH<sub>3</sub>OH line exhibits absorption in a region that covers the full extent of the A1 continuum emission with a size of 0."9. This extended absorption layer is likely associated with the protostellar envelope surrounding the central protostar and possibly its

Table 3

Average Column Density of the Detected Molecules in IRAS 4A

Molecule	$T_{ m rot}$	Column Density	$T_{ m rot}$	Column Density	
	(K)	$N  (\mathrm{cm}^{-2})$	(K)	$N  (\mathrm{cm}^{-2})$	
	IRA	AS 4A2	IRAS 4A1		
CH <sub>3</sub> OH <sup>13</sup> CH <sub>3</sub> OH  CH <sub>2</sub> DOH  CH <sub>3</sub> CHO	200 K <sup>b</sup> ≤375.13 ± 270.02 K 200 K <sup>b</sup> ≤261.31 ± 10.79 K	$\geqslant (5.47 \pm 0.12) \times 10^{17} \text{ a}$ $\geqslant (3.21 \pm 0.30) \times 10^{17}$ $\geqslant (1.30 \pm 0.26) \times 10^{17} \text{ a}$ $\geqslant (3.86 \pm 0.47) \times 10^{16}$	≤140.39 ± 6.63 K ≤58.94 ± 3.74 K 200 K <sup>b</sup> 200 K <sup>b</sup>	$\geqslant (1.14 \pm 0.17) \times 10^{17}$ $\geqslant (1.92 \pm 0.21) \times 10^{15}$ $\geqslant (6.51 \pm 1.83) \times 10^{15}$ $\geqslant (3.2 \pm 0.67) \times 10^{14}$ a	

#### Notes.

circumstellar disk. On the other hand, other COM absorption features from higher upper energy levels ( $\gtrsim$ 40 K) arise from a barely resolved region  $\leq$ 0."25 or  $\leq$ 73 au in diameter.

Based on the rotation diagram analysis in Scenario I, the gas temperature of this more compact absorption layer is  $\sim 100$  K. To have the observed absorption feature produced by a layer of COM (e.g., CH<sub>3</sub>OH gas), a brighter (background) continuum emission is required. Typically, the disk upper layers are hotter due to stellar irradiation, while the midplane is cooler. On the other hand, a high accretion rate can potentially heat up the midplane region, particularly at small radii, and make it hotter than its atmosphere (Dullemond et al. 2007). As illustrated in Figure 7, in this Scenario I, we speculate that we are witnessing a compact path of COM atmosphere absorbing against the very inner and hot part of an inclined circumstellar disk around a protostar at A1. We find, as listed in Table 3, the column density of CH<sub>3</sub>OH at the level of 10<sup>17</sup> cm<sup>-2</sup> (converting <sup>13</sup>CH<sub>3</sub>OH column density). Factoring in a typical fractional abundance of CH<sub>3</sub>OH of  $10^{-6}$  (Herbst & van Dishoeck 2009), the absorbing COM atmosphere will have a column density of  $10^{23}$  cm<sup>-2</sup>. This can be compared to the column density of the "background" continuum disk of 10<sup>26</sup> cm<sup>-2</sup> (see Section 3.1). If the disk is only slightly inclined from face-on, we are able to observe the unresolved, compact (<73 au), hot inner disk and the associated COM atmosphere, which dominates the absorption spectral along its line of sight. The tentative COM absorption features seen by López-Sepulcre et al. (2017) may originate from the same region but get severely beam-diluted at a lower angular resolution. The (optically thick) disk surface has a temperature gradient, which results in an overall (beamaveraged) continuum brightness of 60 K toward the A1 peak. In the case that the level of accretion heating in A1 is not sufficient to elevate the disk midplane temperature above its COM atmosphere locally (i.e., at the same radius), we may be viewing a tilted disk so that along the line of sight, we are seeing an atmosphere against the continuum emission at a smaller radius with higher temperature. Segura-Cox et al. (2018), for example, based on a two-dimensional image fitting of the 8 mm (dust) continuum emission observed with the JVLA, inferred a modestly inclined disk at 35°. The slightly inclined disk probably leads to a seemingly faster but less extended bipolar outflow in A1 as compared to that in A2 (Santangelo et al. 2015), as the outflow will be highly inclined, resulting in a larger velocity along the line of sight and less transverse motion on the plane of the sky. A nearly pole-on (6°) view of a bipolar outflow toward A1 was actually considered

by Santangelo et al. (2015), although a different interpretation was preferred. A nearly face-on disk orientation could explain the lack of a clear velocity gradient seen in NH<sub>3</sub> toward A1 by Choi et al. (2007, 2011). In contrast, a velocity gradient perpendicular to the bipolar outflow was seen in NH<sub>3</sub> toward A2. The lack of an obvious fast rotating signature in NH<sub>3</sub> emission around A1 led Choi et al. (2011) to speculate that A1 hosts a less massive protostar than A2 does.

The geometry of IRAS 4A1 proposed above is close to the picture suggested by Oya et al. (2018) of I16293 B. I16293 is another protobinary where two (sub)millimeter continuum emission cores, I16293 A and B, show hot corino activities (Oya et al. 2016). Similar to the case of IRAS 4A, the weaker continuum of I16293 (i.e., A core) shows richer COM (emission) features compared to that of the B core. Zapata et al. (2013) revealed a compact structure from continuum emission (0.45 mm, angular resolution  $\sim$ 0"2) of I16293 B and revealed a pronounced inner depression or absorption hole from H<sup>13</sup>CN, HC<sup>15</sup>N, and CH<sub>3</sub>OH images. The "hole" size is comparable to the continuum size, which is optically thick. So, in that image, the molecular emission is surrounded by a wall. Our observation has little similarity with this case, but in our case we do not find any molecular emission outside the central beam. The outer disk (beyond 36 au in radius) is probably cold or optically thick, so COM emission is absent, due to a lack of COMs in the gas phase or to attenuation of line emissions by the continuum. A relevant case related to this picture is the COM environment observed in the HH212 system (Lee et al. 2017b). COMs were observed above the disk surface but not in the optically thick disk (Lee et al. 2017a) itself in HH212.

It is interesting to note that emissions of complex organics such as CH<sub>3</sub>OH, CH<sub>2</sub>DOH, HCOOCH<sub>3</sub>, and NH<sub>2</sub>CHO have been proposed to trace the centrifugal barrier of accretion disks (Lee et al. 2017b; Oya et al. 2018). In the case of HH212, Lee et al. (2017b) observed a couple of layers of hot COM gas, including CH<sub>3</sub>OH, CH<sub>2</sub>DOH, and NH<sub>2</sub>CHO, above and below an edge-on disk. The extent of the COM "atmosphere" is consistent with that of a centrifugal barrier (CB) at 44 au based on kinematics considerations. For I16293 B, compact CH<sub>3</sub>OH and HCOOCH3 emissions were observed toward its continuum; it was also suggested to trace the CB at a radius of 40 au. If our observed COM emission is indeed associated with the same phenomenon, the compact nature of the COM absorption in A1 would imply that there is only a small  $(\sim 36 \text{ au})$  disk within which Keplerian rotation has been established. We have not seen all of the molecular transitions

<sup>&</sup>lt;sup>a</sup> For multiple transitions where there is no available rotational temperature, the average column density is for the assumed temperature.

<sup>&</sup>lt;sup>b</sup> Rotational temperature is not available; this is the assumed value. The errors in the table are for fitting only; there is a calibration error of  $\sim 10\%$ , but we have not included it here.

that are observed toward A2 in the absorption toward A1 (see Figure 2). The difference perhaps indicates that COM emission from A2 has a "genuine" or "typical" hot corino nature, while that from A1 is accretion shock related at CB.

In addition to Scenario I, in which the absorption lines are considered optically thin, we discuss also an alternative scenario (Scenario II). It is possible that some (or all) of the absorption features toward A1 are in fact optically thick and saturated. As shown in Equations (2) and (4) in the optically thick situation, the depth of the absorption line core will be the temperature difference between the background continuum brightness and the foreground absorbing gas temperature, or equivalently, the brightness at the absorption line core is equal to the foreground absorbing gas temperature. In Scenario II, in which invoking a beam-filling factor is not necessary, the absorption lines with different excitation temperatures form at different layers in a temperature-stratified envelope, a configuration illustrated in Figure 7. The lower excitation line saturates at the outer cooler layer, while the higher excitation transition (not excited at the outer layer) becomes optically thick in the relatively inner and hotter region. The CH<sub>3</sub>OH transitions toward A1, for example, probe layers between 30 and 60 K. Considering an envelope with its gas temperature scaling with  $r^{-0.5}$ , where r is the radius from the center protostellar object, a factor of two difference in temperature translates to a radius difference by a factor of four. The velocity for gas, if freefalling at 50 au around a  $0.1\,M_\odot$  protostar, is nearly  $2 \text{ km s}^{-1}$  and would be scaled by  $r^{-0.5}$ . Our observations should be able to detect such (differential) velocity offsets if the gas is under freefall. As suggested in Section 3.2, the consistency of the absorption line velocities with the systematic velocity and among themselves appears to indicate a lack of gas accretion/inflow motion (along the line of sight) in the envelope at the scale of tens of astronomical units.

#### 4.3. Deuterium Fractionation

Now we consider the deuterium fractionation of CH<sub>3</sub>OH in A1 and A2. As CH<sub>3</sub>OH emission in A2 is optically thick, it would be good to compare <sup>13</sup>CH<sub>3</sub>OH and CH<sub>2</sub>DOH column densities in both of the cores. The <sup>13</sup>CH<sub>3</sub>OH/CH<sub>2</sub>DOH ratio for A2 and A1 is 2.47 and 0.29 (considering the average value), respectively. Bianchi et al. (2017) used <sup>13</sup>CH<sub>3</sub>OH to calculate <sup>12</sup>CH<sub>3</sub>OH abundance, and from this they reported a D/H ratio  $\simeq 2 \times 10^{-2}$  for methanol in HH212. The deuterium fractionation is one order lower than typical D/H values in hot cores and prestellar clouds. The observation by Bianchi et al. (2017) was a high-resolution ALMA observation on the scale of 45 au, similar to the scale of current observations,  $\sim$ 73 au. If we consider  $^{12}\text{C}/^{13}\text{C} \sim 70$  (Sheffer et al. 2007; note: the  $^{12}\text{C}/^{13}\text{C}$ ratio is not standard and varies in different media, e.g., Wirström et al. 2011; Taniguchi et al. 2016), then the lower limit of the CH<sub>2</sub>DOH/CH<sub>3</sub>OH ratio in A2 and A1 becomes  $0.6 \times 10^{-2}$  and  $4.9 \times 10^{-2}$ , respectively. This is only a factor of about eight difference in deuteration between the cores A1 and A2. There is a caveat in this calculation: we assume a likely value of rotational temperature (200 K) for this. There is also huge uncertainty in the <sup>13</sup>CH<sub>3</sub>OH column density calculation, and the rotational temperatures of <sup>13</sup>CH<sub>3</sub>OH for the two cores are very different. However, if we consider the result, then it suggests that a higher gas temperature in the hot corino environment indirectly reduces the deuteration in methanol compared to cold prestellar conditions; this is similar to the

methanol deuteration in HH212. It may imply that A1 also has a hot environment like A2 with similar deuterium fractionation and hosts a hot corino.

#### 5. Conclusion

We have observed the NGC 1333 IRAS 4A protobinary system with its two cores, A1 and A2, well resolved using ALMA. The results can be summarized as follows:

- 1. The dust continuum emission toward the core A2 is found to be predominantly optically thin at this scale, while the continuum emission toward A1 is most likely to be optically thick.
- 2. A forest of spectral line emissions is observed toward A2, while spectral transitions toward A1 are detected in absorption. Here we have identified and discussed some COMs like CH<sub>3</sub>OH, <sup>13</sup>CH<sub>3</sub>OH, CH<sub>2</sub>DOH, and CH<sub>3</sub>CHO in both cores A1 and A2. The A2 core is a known hot corino with a rich presence of COMs.
- 3. The observed absorption features toward A1 are probably arising from a hot-corino-like atmosphere against a very compact (≤36 au) disk in A1. We speculate that this compact hot-corino-like atmosphere may resemble the cases in HH212 and I16293 B, in which the COM emission is related to the centrifugal barrier of accretion disks. Alternatively, the absorption may arise from different layers of a temperature-stratified, dense envelope.
- 4. An indirect calculation of deuterium fractionation shows that the  $CH_2DOH/CH_3OH$  ratio has a similar order ( $\sim 10^{-2}$ ) toward both of the sources. This low deuterium fractionation in both sources may imply a hot gas condition ( $\sim 100 \text{ K}$ ) typical of a hot corino.

We thank Prof. Emmanuel Caux for helpful discussion and suggestions and Dr. Kuo-Song Wang and Dr. Tien-Hao Hsieh (ASIAA, Taiwan) for some technical help. D.S. wants to thank ASIAA, Taiwan, for providing a visitor position and computational facility and also wishes to thank PRL, India, for support with the international travel grant. D.S. also acknowledges IIA, India for supporting the research (IIA-PDF). S.Y.L. acknowledges the support by the Minister of Science and Technology of Taiwan (MOST 107-2119-M-001-041). Z.Y.L. is supported in part by NSF grants AST-1815784 and AST-1716259 and NASA grants 80NSSC18K1095 and NNX14AB38G. S.T. acknowledges a grant from the Ministry of Science and Technology (MOST) of Taiwan (MOST 102-2119-M-001-012-MY3), and JSPS KAKENHI grant Nos. JP16H07086 and JP18K03703 in support of this work. This work was supported by NAOJ ALMA Scientific Research grant No. 2017-04A. This paper makes use of the following ALMA data: ADS/ JAO.ALMA#2015.1.00147.S. ALMA is a partnership of ESO (representing its member states), NSF (USA), and NINS (Japan), together with NRC (Canada) and MoST and ASIAA (Taiwan) and KASI (Republic of Korea), in cooperation with the Republic of Chile. The Joint ALMA Observatory is operated by ESO, AUI/NRAO, and NAOJ.

## **ORCID** iDs

Sheng-Yuan Liu https://orcid.org/0000-0003-4603-7119 Chin-Fei Lee https://orcid.org/0000-0002-3024-5864 Shigehisa Takakuwa https://orcid.org/0000-0003-0845-128X

#### References

```
Awad, Z., Viti, S., Collings, M. P., & Williams, D. A. 2010, MNRAS,
  407, 2511
Bacmann, A., Taquet, V., Faure, A., Kahane, C., & Ceccarelli, C. 2012, A&A,
  541, L12
Balucani, N., Ceccarelli, C., & Taquet, V. 2015, MNRAS, 449, L16
Barone, V., Latouche, C., Skouteris, D., et al. 2015, MNRAS, 453, L31
Bianchi, E., Codella, C., Ceccarelli, C., et al. 2017, A&A, 606, L7
Bisschop, S. E., Jørgensen, J. K., Bourke, T. L., Bottinelli, S., &
  van Dishoeck, E. F. 2008, A&A, 488, 959
Blake, G. A., Sutton, E. C., Masson, C. R., & Phillips, T. G. 1987, ApJ,
  315, 621
Bottinelli, S., Ceccarelli, C., Lefloch, B., et al. 2004, ApJ, 615, 354
Bottinelli, S., Ceccarelli, C., Williams, J. P., & Lefloch, B. 2007, A&A,
   463, 601
Brown, W. A., & Bolina, A. S. 2007, MNRAS, 374, 1006
Cazaux, S., Tielens, A. G. G. M., Ceccarelli, C., et al. 2003, ApJL, 593, L51
Charnley, S. B., Tielens, A. G. G. M., & Millar, T. J. 1992, ApJL, 399, L71
Choi, M., Kang, M., Tatematsu, K., et al. 2011, PASJ, 63, 1281
Choi, M., Tatematsu, K., & Kang, M. 2010, ApJL, 723, L34
Choi, M., Tatematsu, K., Park, G., & Kang, M. 2007, ApJL, 667, L183
Codella, C., Ceccarelli, C., Cabrit, S., et al. 2016, A&A, 586, L3
Comito, C., Schilke, P., Phillips, T. G., et al. 2005, ApJS, 156, 127
Cox, E. G., Harris, R. J., Looney, L. W., et al. 2015, ApJL, 814, L28
Crockett, N. R., Bergin, E. A., Neill, J. L., et al. 2014, ApJ, 787, 112
Di Francesco, J., Myers, P. C., Wilner, D. J., Ohashi, N., & Mardones, D. 2001,
   ApJ, 562, 770
Drozdovskaya, M. N., Walsh, C., Visser, R., Harsono, D., & van Dishoeck, E. F.
   2015, MNRAS, 451, 3836
Dullemond, C. P., Hollenbach, D., Kamp, I., & D'Alessio, P. 2007, in
   Protostars and Planets V, ed. B. Reipurth, D. Jewitt, & K. Keil (Tucson:
   Univ. Arizona Press), 555
Fuente, A., Cernicharo, J., Caselli, P., et al. 2014, A&A, 568, A65
Garrod, R. T., & Herbst, E. 2006, A&A, 457, 927
Geppert, W. D., Hamberg, M., Thomas, R. D., et al. 2006, FaDi, 133, 177
Goldsmith, P. F., & Langer, W. D. 1999, ApJ, 517, 209
Herbst, E., & van Dishoeck, E. F. 2009, ARA&A, 47, 427
Hirota, T., Bushimata, T., Choi, Y. K., et al. 2008, PASJ, 60, 37
Imai, M., Sakai, N., Oya, Y., et al. 2016, ApJL, 830, L37
Jaber, A. A., Ceccarelli, C., Kahane, C., & Caux, E. 2014, ApJ, 791, 29
Jennings, R. E., Cameron, D. H. M., Cudlip, W., & Hirst, C. J. 1987, MNRAS,
Jiménez-Serra, I., Vasyunin, A. I., Caselli, P., et al. 2016, ApJL, 830, L6
Jørgensen, J. K., Bourke, T. L., Myers, P. C., et al. 2005, ApJ, 632, 973
Jørgensen, J. K., Bourke, T. L., Myers, P. C., et al. 2007, ApJ, 659, 479
Jørgensen, J. K., Bourke, T. L., Nguyen Luong, Q., & Takakuwa, S. 2011,
   A&A, 534, A100
Jørgensen, J. K., Favre, C., Bisschop, S. E., et al. 2012, ApJL, 757, L4
Jørgensen, J. K., van der Wiel, M. H. D., Coutens, A., et al. 2016, A&A,
  595, A117
Karska, A., Herczeg, G. J., van Dishoeck, E. F., et al. 2013, A&A, 552, A141
Kramer, C., Alves, J., Lada, C., et al. 1998, A&A, 329, L33
Kristensen, L. E., van Dishoeck, E. F., Bergin, E. A., et al. 2012, A&A,
Kuan, Y.-J., Huang, H.-C., Charnley, S. B., et al. 2004, ApJL, 616, L27
Lay, O. P., Lay Carlstrom, J. E., & Hills, R. E. 1995, ApJL, 452, L73
Lee, C.-F., Li, Z.-Y., Ho, P. T. P., et al. 2017a, SciA, 3, e1602935
Lee, C.-F., Li, Z.-Y., Ho, P. T. P., et al. 2017b, ApJ, 843, 27
Li, J. I., Liu, H. B., Hasegawa, Y., & Hirano, N. 2017, ApJ, 840, 72
Liu, H. B., Lai, S.-P., Hasegawa, Y., et al. 2016, ApJ, 821, 41
Looney, L. W., Mundy, L. G., & Welch, W. J. 2000, ApJ, 529, 477
López-Sepulcre, A., Jaber, A. A., Mendoza, E., et al. 2015, MNRAS, 449, 2438
```

```
López-Sepulcre, A., Sakai, N., Neri, R., et al. 2017, A&A, 606, A121
McMullin, J. P., Waters, B., Schiebel, D., Young, W., & Golap, K. 2007, in
   ASP Conf. Ser. 376, Astronomical Data Analysis Software and Systems
  XVI, ed. R. A. Shaw, F. Hill, & D. J. Bell (San Francisco, CA: ASP), 127
Millar, T. J., Herbst, E., & Charnley, S. B. 1991, ApJ, 369, 147
Mottram, J. C., van Dishoeck, E. F., Schmalzl, M., et al. 2013, A&A,
  558, A126
Müller, H. S. P., Schlöder, F., Stutzki, J., & Winnewisser, G. 2005, JMoSt,
   742, 215
Müller, H. S. P., Thorwirth, S., Roth, D. A., & Winnewisser, G. 2001, A&A,
Öberg, K. I., Guzmán, V. V., Furuya, K., et al. 2015, Natur, 520, 198
Öberg, K. I., Lauck, T., & Graninger, D. 2014, ApJ, 788, 68
Öberg, K. I., van der Marel, N., Kristensen, L. E., & van Dishoeck, E. F. 2011,
   ApJ, 740, 14
Ortiz-León, G. N., Loinard, L., Dzib, S. A., et al. 2018, ApJ, 865, 73
Oya, Y., Moriwaki, K., Onishi, S., et al. 2018, ApJ, 854, 96
Oya, Y., Sakai, N., López-Sepulcre, A., et al. 2016, ApJ, 824, 88
Palau, A., Walsh, C., Sanchez-Monge, A., et al. 2017, MNRAS, 467, 2723
Park, G., & Choi, M. 2007, ApJL, 664, L99
Persson, M. V., Jørgensen, J. K., & van Dishoeck, E. F. 2012, A&A, 541, A39
Pickett, H. M., Poynter, R. L., Cohen, E. A., et al. 1998, JOSRT, 60, 883
Sahu, D., Minh, Y.-C., Lee, C.-F., et al. 2018, MNRAS, 475, 5322
Sakai, N., Sakai, T., Hirota, T., Burton, M., & Yamamoto, S. 2009, ApJ,
  697, 769
Sakai, N., Sakai, T., Hirota, T., & Yamamoto, S. 2008, ApJ, 672, 371
Sakai, N., Sakai, T., Hirota, T., & Yamamoto, S. 2010, ApJ, 722, 1633
Sakai, N., Sakai, T., & Yamamoto, S. 2006, PASJ, 58, L15
Sandell, G., Aspin, C., Duncan, W. D., Russell, A. P. G., & Robson, E. I. 1991,
   ApJL, 376, L17
Sandell, G., & Knee, L. B. G. 2001, ApJL, 546, L49
Santangelo, G., Codella, C., Cabrit, S., et al. 2015, A&A, 584, A126
Sault, R. J., Teuben, P. J., & Wright, M. C. H. 1995, in ASP Conf. Ser. 77, in
   Astronomical Data Analysis Software and Systems IV, ed. R. Shaw,
  H. E. Payne, & J. J. E. Hayes (San Francisco, CA: ASP), 433
Segura-Cox, D. M., Looney, L. W., Tobin, J. J., et al. 2018, ApJ, 866, 161
Sheffer, Y., Rogers, M., Federman, S. R., et al. 2007, ApJ, 667, 1002
Shepherd, D. S., & Watson, M. 2002, ApJ, 566, 966
Smith, K. W., Bonnell, I. A., Emerson, J. P., & Jenness, T. 2000, MNRAS,
  319, 991
Sugimura, M., Yamaguchi, T., Sakai, T., et al. 2011, PASJ, 63, 459
Taniguchi, K., Saito, M., & Ozeki, H. 2016, ApJ, 830, 106
Taquet, V., López-Sepulcre, A., Ceccarelli, C., et al. 2015, ApJ, 804, 81
Tercero, B., Cernicharo, J., Pardo, J. R., & Goicoechea, J. R. 2010, A&A,
  517, A96
Tielens, A. G. G. M. 2005, The Physics and Chemistry of the Interstellar
  Medium (Cambridge: Cambridge Univ. Press)
Tielens, A. G. G. M., & Hagen, W. 1982, A&A, 114, 245
Turner, B. E. 1991, ApJS, 76, 617
van der Tak, F. F. S. 2004, in Proc. IAU Symp. 221, Star Formation at High
  Angular Resolution, ed. M. G. Burton, R. Jayawardhana, & T. L. Bourke
  (Dordrecht: Kluwer), 59
van't Hoff, M. L. R., Tobin, J. J., Trapman, L., et al. 2018, ApJL, 864, L23
Vastel, C., Ceccarelli, C., Lefloch, B., & Bachiller, R. 2014, ApJL, 795, L2
Walsh, C., Loomis, R. A., Öberg, K. I., et al. 2016, ApJL, 823, L10
Wirström, E. S., Geppert, W. D., Hjalmarson, Å., et al. 2011, A&A, 533, A24
Yıldız, U. A., Acharyya, K., Goldsmith, P. F., et al. 2013, A&A, 558, A58
Zapata, L. A., Ho, P. T. P., Rodríguez, L. F., Schilke, P., & Kurtz, S. 2007,
   A&A, 471, L59
Zapata, L. A., Loinard, L., Rodríguez, L. F., et al. 2013, ApJL, 764, L14
Zapata, L. A., Schmid-Burgk, J., Ho, P. T. P., Rodríguez, L. F., &
  Menten, K. M. 2009, ApJL, 704, L45
Zucker, C., Schlafly, E. F., Speagle, S. F., et al. 2018, ApJ, 869, 83
```